



Cite this: *Soft Matter*, 2015, 11, 4540

# Superhydrophobic and anti-icing properties at overcooled temperature of a fluorinated hybrid surface prepared *via* a sol–gel process

Yongqiang Tang, Qinghua Zhang,\* Xiaoli Zhan and Fengqiu Chen

A superhydrophobic surface with anti-icing performance has been the focus of research, but few studies have reported the effective and low cost strategy that met the requirements under overcooled conditions. In this article, the fluorinated sol–gel colloid coatings were simply prepared *via* hydrolytic condensation of nanosilica sol, methyltriethoxysilane (MTES) and 3-[(perfluorohexylsulfonyl)amino]propyltriethoxysilane (HFTES). The multi scale morphology and chemical composition of the artificial surfaces were characterized by scanning electron microscopy (SEM), atomic force microscopy (AFM) and X-ray photoelectron spectroscopy (XPS). The influence of the surface roughness structure and fluorinated groups on the wettability and freezing delay time of the colloid surface under overcooled conditions were explored. As the HFTES content was higher than 6 wt%, the prepared colloid surface showed excellent superhydrophobicity with a contact angle (CA) of about 166° at room temperature. The CA gradually reduced with the decrease of the temperature. Only the samples with high HFTES contents (above 30 wt%) exhibited special superhydrophobic and anti-icing properties under freeze temperature. Besides the surface roughness structure, the high fluoride enrichment on the surface plays a major role in the superhydrophobic and anti-icing properties under overcooled conditions.

Received 23rd March 2015,  
Accepted 5th May 2015

DOI: 10.1039/c5sm00674k

www.rsc.org/softmatter

## 1. Introduction

Once air temperature is below the freezing point, the adherent raindrops on solid surfaces will convert into ice. The ice buildup on solid surfaces caused by freezing rain and snow during cold weather in moist regions creates serious problems on facilities, power supplies, telecommunication networks and wind turbines, leading to safety and energy efficiency considerations.<sup>1,2</sup> Therefore, reducing the impact of the ice storm on the substrate has become a critical task need to be solved urgently. The commonly used ice removal strategies, such as heating, spraying deicing fluid and mechanical means, have several drawbacks due to the detrimental environmental consequences and energy consumption.<sup>3</sup> The special anti-icing coating based on preventing ice formation and reducing ice adhesion strength has attracted extensive interests.<sup>4–7</sup> An ideal anti-icing coating should have two characteristics. One is that overcooled water droplets could roll off the surface easily before crystallization. The other is that the ice adhesion should be weaker when ice is accumulated on the surface.<sup>8</sup>

Inspired by the lotus effect,<sup>9</sup> superhydrophobic surfaces with a contact angle (CA) higher than 150°<sup>10</sup> and a low contact angle

hysteresis (CAH)<sup>11</sup> have received tremendous attention recently.<sup>12–15</sup> Many artificial superhydrophobic surfaces have been fabricated by creating surface morphology with a micro-nano composite structure and introduction of low surface energy groups.<sup>16–18</sup> Construction of a rough surface is well known to be vitally important for fabrication of an artificial superhydrophobic surface. It has been proven that a dual-scale roughness structure is a predominant feature in creating a superhydrophobic surface and especially important for obtaining low water sliding angle (SA).<sup>19,20</sup> Based on these processes, various methods have been applied in preparing superhydrophobic surfaces such as a layer-by-layer assembling method,<sup>21,22</sup> chemical vapor deposition,<sup>23,24</sup> etching processing,<sup>25,26</sup> the electrochemistry method<sup>12,27</sup> and so on. However, many of these methods involve multistep procedures or specialized equipments with difficult process controls. The other methods may require multiple steps and are not suitable for large area applications.<sup>28</sup>

It is urgent to develop a simple method to efficiently prepare a superhydrophobic surface. The sol–gel process is considered a facile method for fabrication of superhydrophobic surface with a controlled roughness structure.<sup>29</sup> In recent years, a great deal of research has been carried out to develop superhydrophobic surfaces *via* the sol–gel method with different precursors, such as fluorinated alkyl silane (FAS)<sup>30–33</sup> and any other nonfluorinated co-precursors.<sup>29,34,35</sup> This organic–inorganic hybrid material

College of Chemical and Biochemical Engineering, Zhejiang University, Hangzhou 310027, P. R. China. E-mail: qhzhzhang@zju.edu.cn; Fax: +86 571 87991227

has other fascinating performance which cannot be obtained by mixing inorganic nanoparticles with organic resin. The organic parts provide a controlled molecular structure and good processability, while the inorganic parts offer a high modulus and wonderful thermal and mechanical stability. Based on these remarkable physicochemical properties, the organic–inorganic hybrid material is applied in various fields such as nanomaterials, optoelectronic devices, biology, and so on.<sup>36</sup>

Though many artificial superhydrophobic surfaces exhibited obvious anti-icing or icephobic properties, the standpoint that the superhydrophobic surfaces are best for use as ice-repellents is suffering many queries from academia.<sup>37,38</sup> The doubts about the anti-icing property of the superhydrophobic surface are presented in two ways. One is that most superhydrophobic surfaces lose part or all of their superhydrophobicity under overcooled conditions, such as in the weather of freezing rain and wet snow.<sup>39</sup> The other is that the dual micro-nano structure being easily damaged in the deicing process is very difficult to repair. How to keep superhydrophobic performance by controlling the roughness structure and chemical composition under freeze temperatures is more important for practical anti-icing applications. Unfortunately, the artificial surfaces maintaining nearly the same superhydrophobic character under normal and overcooled environment are still rare. More studies focused on the construction of the micro-nano roughness structure for preparation of the superhydrophobic surface, while the role of surface chemical groups had often been ignored.<sup>16,29</sup> Few researchers provide thorough understanding on the anti-icing performance of such superhydrophobic surfaces in overcooled temperature.<sup>40</sup>

In this paper, we present a simple sol–gel method to prepare a superhydrophobic surface *via* hydrolytic condensation of nanosilica sol, methyltriethoxysilane (MTES) and a fluorine contained compound (HFTES). Multiscale roughness structures were achieved by controlling the content of nanosilica sol in the mixture. The hydrophobicity of the nanocomposite materials determined by the surface roughness and chemical composition with low surface energy were discussed. Furthermore, the superhydrophobic performance and the wettability mechanism of the prepared hybrid surface under low temperature were explored. The delay time of the water droplet freezing in overcooled surroundings and the anti-icing behaviors of droplets on the superhydrophobic surface were discussed based on the classical heterogeneous nucleation. In addition, the classic “cross-hatch” test and icing/icing-melting cycle process were applied to check the adhesion and durability of the coatings.

## 2. Experimental

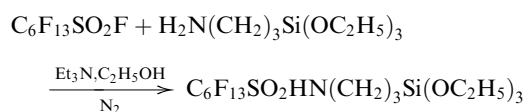
### 2.1 Materials

Nanosilica sol (CR-23-IPA, solid content 30 wt%, 2-propanol dispersion solution) was purchased from Zhangjiagang Chosen Technology Co., Ltd, the diameter of nanosilica particles is on average 20 nm. 1-Hexanesulfonyl fluoride was provided by Hubei Hengxin Chemical Co., Ltd.  $\gamma$ -Aminopropyltriethoxysilane (APTES)

was purchased from Aldrich Chemical Co. Methyltriethoxysilane (MTES) was purchased from Aldrich Chemical Co. and was diluted into 30 wt% with 2-propanol. 2-Propanol and other reagents were obtained from Sinopharm Chemical Reagent Co. and used without any further purification. Hydrochloric acid (36 wt%) was purchased from Sinopharm Chemical Reagent Co. and was diluted to 1 wt% with deionized water.

### 2.2 Preparation of fluorinated silane with a short perfluoroalkyl chain

The approach to prepare 3-[(perfluorohexylsulfonyl)amino]-propyltriethoxysilane (HFTES) is shown in the following equation.<sup>41</sup>



Typically, 8.2 g of APTES, 25 mL of ethanol and 5.1 g of triethylamine were placed in a 250 mL round flash equipped with a mechanical stirrer and a reflux condenser. Before the reaction started, the flask was purged with nitrogen for 30 min in order to remove the oxygen. Then the flask was placed in a constant temperature water bath at 9 °C and 14.9 g of 1-hexanesulfonyl fluoride was added to this mixture solution, drop by drop, while stirring constantly. After that, the solution was stirred at 45 °C for another 2 h. Distillation was needed for purification before getting a canary yellow product, with a yield of 90%.

### 2.3 Preparation of fluorinated sol–gel nanocomposite films

Variable amounts of nanosilica sol were added in the mixture of MTES and HFTES by magnetic stirring at 30 °C. Then, a certain amount of HCl solution was dropwise added into this solution and stirred constantly for 30 min. After that, the obtained fluorinated sol was spin-coated onto clean glass slides at room temperature using a chemical technology KW-4A spinning coater. A rotational speed of 1500 rpm and a holding time of 1 min were chosen. The samples were evaporated slowly for a day and then thermally treated at 150 °C for 1 h.

### 2.4 Surface structure and composition analysis of the composite films

FTIR spectra of fluorinated silane with a short perfluoroalkyl chain (HFTES) were measured on a Nicolet 5700 FT-IR spectrometer. In order to investigate the morphology of the prepared samples, SEM analysis was carried out by means of a Hitachi TM-1000 scanning electron microscope at an accelerating voltage of 20 kV. AFM was operated by Multi Mode (Veeco, USA) in tapping mode. The scanning range was 1  $\mu\text{m} \times 1 \mu\text{m}$  but 5  $\mu\text{m} \times 5 \mu\text{m}$  for HFTES-6 wt%–SiO<sub>2</sub>-0 wt% sample. The chemical composition was analyzed by XPS (Thermo Scientific, USA) with an Al K $\alpha$  X-ray source. The X-ray gun was operated at 14 kV and 350 mW, and the analyzer chamber pressure was 10<sup>−9</sup> to 10<sup>−10</sup> Pa.

## 2.5 Surface wettability test

CA for the fluorinated colloid surfaces were measured from  $-20\text{ }^{\circ}\text{C}$  to  $20\text{ }^{\circ}\text{C}$  (relative humidity of 40%) through the sessile drop method using a CAM 200 optical contact-angle goniometer (KSV Instruments, Helsinki Finland). The fluorinated surface was cooled to a certain temperature. And then a water droplet was placed on it. CAH and SA were measured by tilting the sample stage from zero to a higher angle until the droplet rolled off the surface, then the sliding angle was measured, and the advanced angle and receding angle can be calculated. The volume of the tested water droplet is  $2\text{ }\mu\text{L}$ .

## 2.6 Anti-icing measurement

The anti-icing behavior of the prepared hybrid material surfaces and uncoated glass was characterized by the investigation of freezing delay times with a relative humidity of 40%.  $2\text{ }\mu\text{L}$  sized water droplets having an initial temperature of about  $0\text{ }^{\circ}\text{C}$  were sprayed onto the sample surfaces through sprinklers. The temperature of the film samples and substrate were kept constant at  $-20\text{ }^{\circ}\text{C}$ . Freezing delay times were defined as the time between the first droplet impact and the onset of freezing, as determined by direct imaging through a microscope. The onset of freezing coincided with clouding of the water volume, as caused by spontaneous crystallization. The photos of surface freezing were taken every 100 s.

The wettability and anti-icing tests by applying 10 icing/ice-melting cycles were used to test the durability of the coatings. After anti-icing measurement, the frozen sample was placed in room temperature to allow the ice to melt and dried at  $150\text{ }^{\circ}\text{C}$  for 1 h before the next cycle of CA, SA and freezing delay time tests.

## 2.7 Adhesion test

The cross-hatch test based on ASTM D3359 was used to classify the adhesion strength of coatings to the Al sheet as described in the literature.<sup>42</sup> Cross-hatch grids were created according to ASTM D3359-97 in the gauge section of the specimen. A blade with multiple cutting edges spaced 1.5 mm apart was used to create the grids. The first cut was made along the length of the gauge section. The second cut was made at  $90^{\circ}$  to the first cut along the width of the gauge section creating a cross-hatch grid pattern with 210 squares of  $1.5 \times 1.5\text{ mm}$ .

# 3. Results and discussions

## 3.1 Synthesis and characterization of the fluorinated sol-gel composite film

As we know, the perfluoroalkyl compounds with more than eight fluorinated carbon atoms exhibited excellent low surface energy due to the crystallinity of the perfluoroalkyl groups on the surface.<sup>43,44</sup> Most of the artificial fluorinated hybrid materials with superhydrophobic performance were prepared by using long-chain fluorinated compounds. Unfortunately, a long perfluoroalkyl chain, such as perfluorooctyl or perfluorooctanesulfonyl groups, can break down to form perfluorooctanoic acid

(PFOA) and perfluorooctanesulfonate (PFOS), which have caused global ecosystem pollution.<sup>45</sup> It has been reported that perfluorinated carboxylic and sulfonate containing chains of six or less perfluorinated carbon atoms do not bioaccumulate in the human body and are not biopersistent. Our previous work showed that the novel fluorinated materials synthesized by environmentally friendly perfluorohexyl chemicals with sulfonamide as a spacer group present liquid crystalline lamellar structures and outstanding dynamic water repellent property.<sup>46</sup> Based on this result, we prepared a new fluorinated silane with a perfluorohexyl group by reaction of perfluorohexanesulfonyl fluoride with  $\gamma$ -aminopropyltriethoxysilane.

The fluorinated silane was synthesized in ethanol by the method as described in the literature.<sup>41</sup> The chemical structure of the perfluorohexyl silane was identified by FTIR spectra. Fig. 1 shows the FTIR spectra of 3-[(perfluorohexylsulfonyl)amino]propyltriethoxysilane. As seen from Fig. 1, the characteristic absorption of  $\text{S}=\text{O}$  ( $1315\text{ cm}^{-1}$ ),  $\text{C}-\text{F}$  stretch ( $1248\text{ cm}^{-1}$ ),  $\text{Si}-\text{OR}$  ( $1140\text{ cm}^{-1}$ ) and  $\text{Si}-\text{CH}_2$  ( $800\text{ cm}^{-1}$ ) is clearly visible. The weak band observed at about  $3450\text{ cm}^{-1}$  is attributed to the presence of  $\text{N}-\text{H}$ . Most importantly, the  $\text{S}-\text{N}$  stretching vibration at  $1005\text{ cm}^{-1}$  indicates that a fluorinated group is linked with APTES. All of these results prove that the preparation of 3-[(perfluorohexylsulfonyl)amino]propyltriethoxysilane (HFTES) is successful.

The fluorinated sol-gel colloid coating was prepared *via* a simple sol-gel process by hydrolytic condensation of nanosilica sol, MTES and HFTES. The possible chemical reactions for preparation of this coating are shown in Fig. 2. During this process, the inorganic nanosilica particles with active hydroxyl groups on the surfaces are dispersed uniformly in the mixture solution of MTES and HFTES. The ethoxy groups contained in MTES and HFTES can hydrolyze and generate hydroxyl groups in hydrochloric acid solution. Then, polycondensation reaction occurs between silica colloid nanoparticles and hydrolyzed MTES or hydrolyzed HFTES. At the same time, hydrolyzed MTES may react with hydrolyzed HFTES to form copolymer chains.

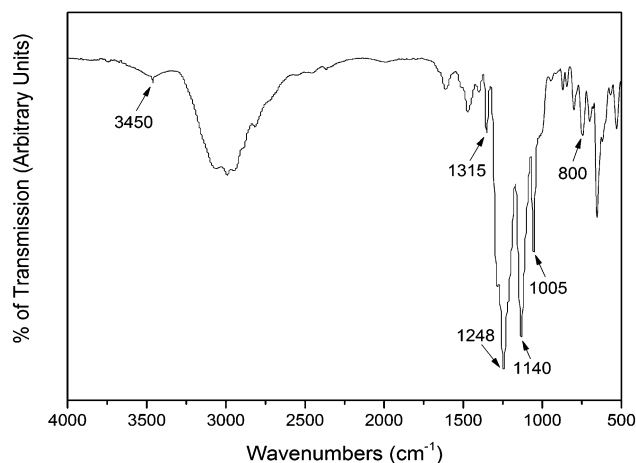


Fig. 1 FTIR spectrum of 3-[(perfluorohexylsulfonyl)amino]propyltriethoxysilane (HFTES).

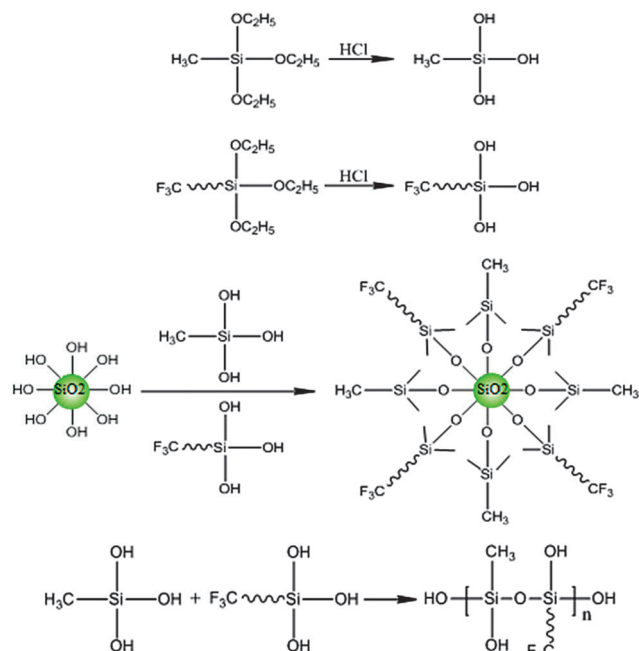


Fig. 2 Schematic of the hydrolyzation of MTES and HFTES and the subsequent polycondensation between the hydrolyzed MTES/HFTES and the nanosilica particles.

As a result, the nanosilica particles are covered by the formed fluorinated copolymer chains, and all of the silica particles are arrested and connected by the polymer networks.<sup>47</sup> After the sol spin-coated on the substrate, heat treatments were followed for the gel formation, which promoted the enrichment of fluorocarbon chains onto the surface of the coating. Thus, a continuous and compact hybrid film with low surface energy was obtained.

### 3.2 Surface roughness of the hybrid colloid film and mechanical adhesion

The surface morphological and roughness structure of the fluorinated colloid film was studied by SEM. Fig. 3 shows the

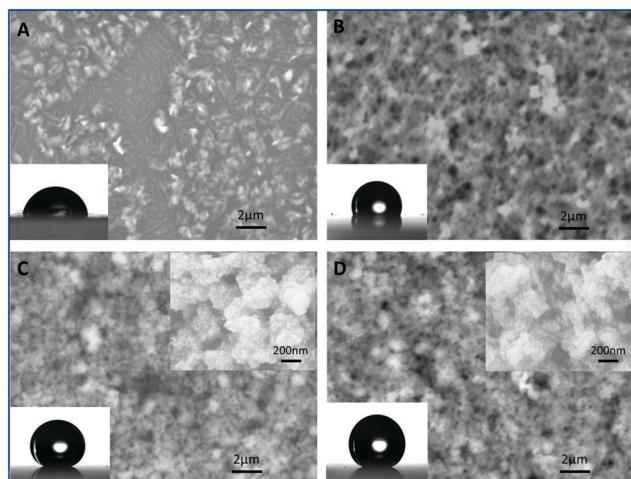


Fig. 3 SEM images of the fluorinated colloid films containing silica sol of (A) 0 wt%, (B) 10 wt%, (C) 30 wt%, (D) 50 wt%.

SEM images of the colloid films containing a HFTES fraction of 6 wt% with different nanosilica sol contents.

By comparing the SEM images of the film samples, we can clearly see that there were great differences between surface morphologies under the same magnification. When no silica sol was added in the solution, as seen in Fig. 3A, the smooth network structure of the colloid film was formed by hydrolytic condensation of MTES and HFTES. With the addition of 10 wt% nanosilica, the obvious aggregation structure for the hybrid colloid film could be obtained (Fig. 3B). When the amount of nanosilica increased from 10 wt% to 50 wt%, the scale of the aggregation structure changed from nano texture to micro-nano composite roughness. As shown in Fig. 3C and D, the agglomerated micro aggregation composed of nano particles can be seen. Therefore, the micro-nano composite roughness was obtained by hydrolytic condensation of MTES and HFTES with addition of adequate nanosilica.

According to SEM analysis, it's confirmed that the roughness of the surface with a dual micro-nano structure could be fabricated by introduction of a nanosilica sol. In this section, tapping mode atomic force microscopy (AFM) was used to further investigate the microstructure of the colloid film. Fig. 4 shows the typical three dimensional AFM height images of the HFTES fraction of 6 wt% contained surfaces with different nanosilica sol contents. The surface topography obtained by AFM images agreed well with the result from SEM characterization. For no silica sol contained coatings (Fig. 4A), it shows a relatively low roughness surface with few dispersed nano aggregates in the scanning range. The root-mean-square (RMS) roughness for this sample is 3.21 nm. Significant changes in the surface morphology are observed after addition of the nanosilica. As shown in Fig. 4B–D, the roughness of the fluorinated colloid surfaces with nanosilica contents of 10 wt%, 30 wt% and 50 wt% are increased to 12.64 nm, 43.80 nm and 44.85 nm, respectively.

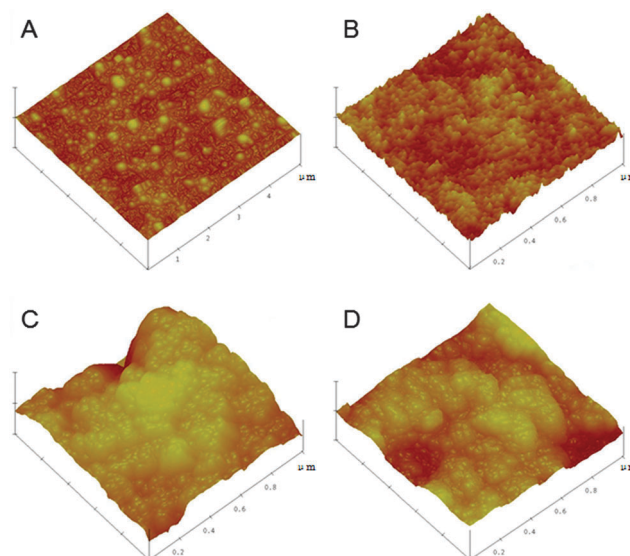


Fig. 4 AFM three-dimensional height images of the fluorinated colloid surfaces containing silica sol of (A) 0 wt%, (B) 10 wt%, (C) 30 wt%, (D) 50 wt%.



**Table 1** HFTES content dependence of adhesion for the sample with 30 wt% silica

HFTES content (wt%)	6	10	30	40
Adhesion	4B	4B	3B	3B

The increase of roughness for the colloid films should be attributed to the aggregation of nanosilica and the formation of the micro-nano roughness structure. From the SEM and AFM images of the samples we can obviously observe the scattered peaks on a relatively flat surface. The small gap between the textural peaks of the roughness is important for the trapping of air pockets.<sup>48</sup> For the prepared hybrid colloid coating, the dual micro-nano structure surface with an increased roughness are fabricated by hydrolytic condensation of nanosilica sol, MTES and fluorinated silane.

A cross-hatch and tape test was performed to check the adhesion strength of the fluorinated hybrid colloid coatings to the Al substrate. The coating adhesion was qualitatively determined from the test result. As shown in Table 1, it can be clearly seen that adhesion of the coatings to the Al substrate is relatively good since all of the adhesion grades of the coatings were above 3B. The values gradually decreased from 4B to 3B with the increasing HFTES content above 30 wt%. due to the relatively weakened crosslinking density caused by the reduction of MTES content.

### 3.3 Hydrophobicity and surface chemical composition of the colloid films

**3.3.1 Influence of nanosilica sol content on hydrophobicity of colloid films at room temperature.** Wettability of the solid material surface is dependent on both the topographical structure and the chemical compositions. The effect of the nanosilica sol content on the surface wetting behavior was investigated by the CA measurements. The test results of the colloid films containing a HFTES fraction of 6 wt% at room temperature are shown in Fig. 5. The CA of water on the film surfaces increased quickly from 78° to 166° with the increasing nanosilica sol content from 0 wt% to 30 wt%. The hydrophobic fluorinated colloid film can be formed by the hydrolytic condensation of MTES and HFTES. With no nanosilica sol participation, the colloid film exhibited a relatively smooth surface with the CA of 78°, which indicated that it is slightly hydrophilic. The possible reason should be that the colloid film formed from condensation of hydrolyzed MTES and HFTES containing a number of hydroxyl groups.

Once the nanosilica sol was added to the system, the colloid film surface changed from smooth to a topological rough structure. As shown in SEM and AFM images (Fig. 3 and 4), the surface of the colloid films changed from nanotextured morphology to a micro-nano multiscale structure with increasing silica content from 10 wt% to 30 wt%. Accordingly, the wettability of the film transformed from an ordinary hydrophobic character with a CA of 115° to a superhydrophobic state with a CA of 166°. When the silica content increased to 50 wt%, the CA on the colloid film remained near 166°. This is because the roughness structures for these colloid films are very similar. The CA

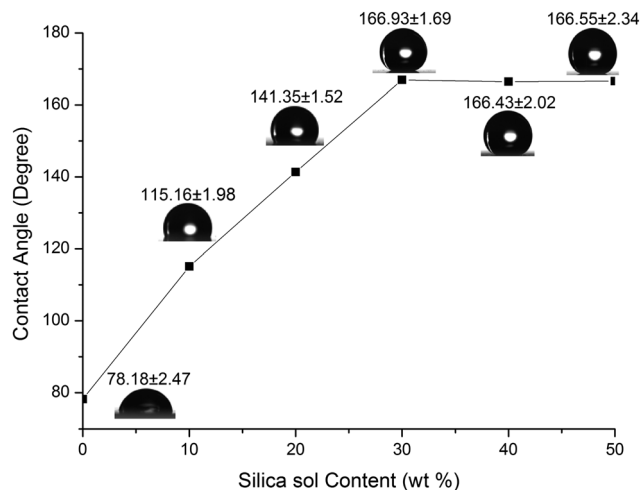


**Fig. 5** Silica sol content dependence of contact angles for the fluorinated sol-gel surfaces. The micrographs show water droplets on the surfaces containing different nanosilica sol contents.

measurements indicated that a superhydrophobic surface was successfully constructed using a facile sol-gel method, and the micro-nano composite structure played a distinctly important role in the preparation of the superhydrophobic surface in a normal environment.

**3.3.2 Influence of fluorinated silane content on the CA at room temperature.** Besides the roughness, the low surface energy groups distributed on the outermost layer is another key factor influencing the superhydrophobic property of the surface. The results in previous research indicates that 30 wt% of silica sol content is appropriate for preparation of a superhydrophobic film with a multiscale composite structure. In this section, we will discuss the influence of fluorinated silane contents on the hydrophobicity of the colloid film with a fixed nanosilica content (30 wt%). Fig. 6 shows the influence of HFTES content

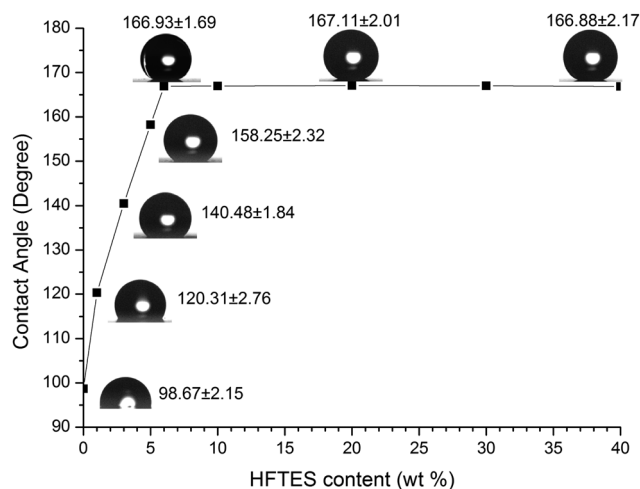


**Fig. 6** HFTES content dependence of contact angles for the colloid surfaces. The micrographs show water droplets on the surfaces containing different HFTES contents.

on the CA of water on the coating surface. RMS roughness of all these surfaces was almost the same ranging from 40 to 50 nm.

For no fluoride contained sample presented in Fig. 6, the colloid film is formed by the hydrolytic condensation of MTES and nanosilica sol. The CA on this colloid film is found to be  $98.67^\circ$ , which shows some hydrophobic property because of the hydrophobic portion of  $-\text{CH}_3$  groups in MTES. With increasing HFTES content, the prepared surface shows enhanced hydrophobicity due to more fluoride contained groups distributed on the outermost surface. When HFTES content reached 6 wt%, the CA on the coating surface can get as high as  $166.93^\circ$ . Then with further increasing fluorinated silane amounts, CA still remained near 166 degrees. The surface covered with high density of perfluoroalkyl chains could exhibit ultra-low surface energy. The combination of a micro-nano composite structure and enrichment of low surface energy fluorinated groups on the surface cause formation of the superhydrophobic surface. To the best of our knowledge, 6 wt% is an extremely low dosage of the fluoride agent to prepare such a superhydrophobic surface *via* the sol-gel method.<sup>30,31</sup> In order to further explore the surface chemical composition of the colloid films, XPS will be applied for quantitative analysis of the prepared coating and determining of the relationship of surface composition and wettability.

**3.3.3 XPS analysis for surface composition of the hybrid film.** The CA measurement indicates that the content of HFTES in the colloid film would affect its hydrophobicity. The quantitative elemental compositions of the fluorine contained colloid samples can be evaluated from XPS results. Fig. 7 displays XPS  $\text{C}1_{\text{p}}$ ,  $\text{Si}2_{\text{p}}$ ,  $\text{O}1_{\text{s}}$  and  $\text{F}1_{\text{s}}$  spectra of the coating films with different HFTES contents. In the XPS analysis, the high binding energy of

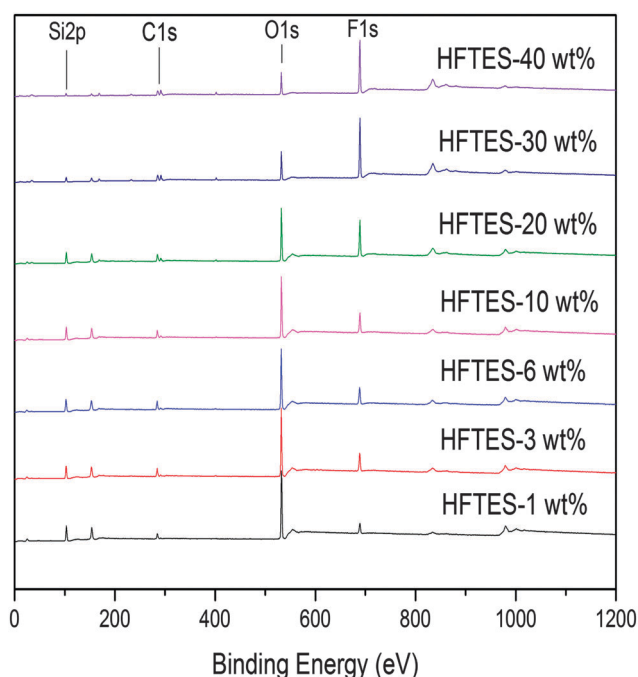


Fig. 7 XPS survey spectra of the colloid surfaces with different HFTES contents.

Table 2 F/C atomic ratio and composition of the colloid coatings containing different HFTES contents

Sample	Molar ratio of HFTES/MTES (%)	F/C atomic ratio (%)	
		Stoichiometric value <sup>a</sup>	Experimental value <sup>b</sup>
HFTES-1 wt%	0.44	0.79	29.75
HFTES-3 wt%	1.33	2.39	31.91
HFTES-6 wt%	2.76	4.85	34.83
HFTES-10 wt%	4.91	8.27	38.76
HFTES-20 wt%	11.83	17.50	46.88
HFTES-30 wt%	22.16	27.89	54.77
HFTES-40 wt%	39.34	32.58	54.74

<sup>a</sup> Calculated on the basis of the known composition of the hybrid film.

<sup>b</sup> The experimental values based on the XPS measurement.

685.5 eV should arise from the F element in the HFTES. With the increasing of HFTES content, the intensity of Si and O peaks decreased while the intensity of F peaks at 685.5 eV increased obviously. The atomic ratios of the surface elements calculated by curve area integrals in XPS spectra are described in Table 2. For all of the samples, the fluorine atomic ratio on the surface was obviously higher than that in the bulk due to the significant surface enrichment of low surface energy groups.

The atomic ratios of F/C in the surface were calculated by curve area integrals in XPS spectra and the F/C value of the bulk was calculated on the known composition. The relationship of the F/C value determined by experiment and the theoretically calculated value in bulk for different films are shown in Fig. 8. It can be seen that the F/C value based on XPS measurement was always higher than that calculated because the fluorocarbon chains tend to migrate to the surface. With increasing HFTES content, the experimental F/C value gradually increased due to more fluorocarbon chains migrating to the surface, and the prepared surface showed an enhanced hydrophobicity. As HFTES content increased from 30 wt% to 40 wt%, the theoretical F/C value in bulk increased from 27.89 to 32.58, while the experimental F/C value on the surface remains at about 54.7,

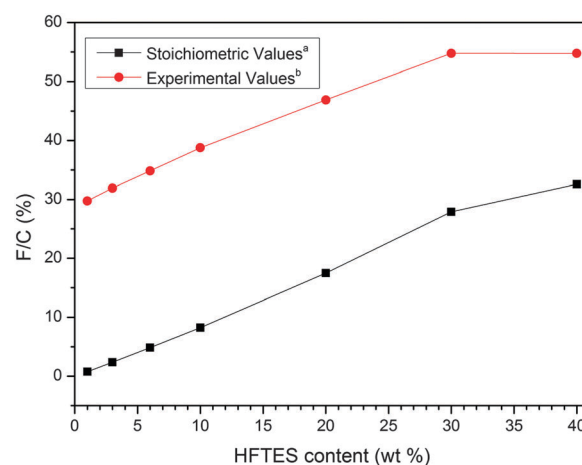


Fig. 8 HFTES content dependence of the F/C atomic ratio. (<sup>a</sup> Calculated on the basis of the known composition of the hybrid film. <sup>b</sup> The experimental values were determined based on the XPS measurement.)

which means the coverage of fluorocarbon groups at the outermost surface saturate at this content. The previous result shows that the CA of water on the colloid film with a HFTES content above 6 wt% can achieve the equilibrium value of about  $166^\circ$ . This phenomenon indicates that the superhydrophobic surface with a Cassie state can be achieved by fabricating a micro-nano composite structure covered with different hydrophobic organic groups at ambient temperature.

### 3.4 Anti-icing property of fluorinated sol-gel colloid surface

The design of an effective ice resistant coating for using in a natural environment requires the optimization of multiple properties of the surface. Anti-icing property mainly refers to easy removal of overcooled water droplets before it freezes and delay in the crystallization. However, most superhydrophobic surfaces lose part or all of their superhydrophobicity under a supercooled environment, such as in the weather of sleet or freezing rain.<sup>8</sup> The anti-icing property of the prepared surface could be characterized by dynamic contact angle measurement in both ambient and subzero condition.

#### 3.4.1 Removal of condensed water before crystallization.

The adhesive force between condensed water and the coating surface is the crucial factor determining whether it is easy for the condensed water to roll off the surface. Lower force makes the removal procedure easier. It's well known that the dominant molecular interactions include Van der Waals interaction, hydrogen bond and hydrophobic forces. Fluorinated groups  $-CF_3$  covered coating is considered an optimized surface because of furthest minimized interaction between the liquid water molecules and the solid surface. Furthermore, the real contact area of the water drop refers to the fraction of the wetted area and the large contact angle means a small contact area. So the force between condensed water and the coating surface can be reduced by increasing CA and reducing CAH or SA.

Table 3 shows the static and dynamic contact angle of the colloid films with different HFTES content. As seen in Table 3, when the content of nanosilica sol was 30 wt%, the CA of water on the film surface increased quickly, while SA and CAH decreased increasing of HFTES content from 0 to 6 wt%. As HFTES content reached 6 wt% and above, CA on the surface achieved as high as about  $166^\circ$ . For a textured superhydrophobic surface,

air can be trapped inside the grooves in the multiscale roughness structure, and the real contact area is generally reduced due to the presence of air layer. On the other hand, with the increasing of HFTES content to above 6 wt%, CAH decreased from  $52.17^\circ$  to below  $8^\circ$  and SA decreased from  $51^\circ$  to below  $6^\circ$ . It can be concluded that the prepared superhydrophobic surface with a sufficient amount of HFTES exhibit ultralow CAH and SA and result in easy removal of condensed water under the effect of outside force.

**3.4.2 Wettability properties of the superhydrophobic surfaces in overcooled environment.** Most of the prepared surfaces with different composition showed the same superhydrophobicity under normal temperature. However, the wettability performance of the surface under a supercooled environment is the critical issue for the anti-icing application. It has been confirmed that the temperature and humidity had a significant effect on the wettability of surfaces. Table 4 describes the CA and SA of water on the prepared superhydrophobic surfaces with different HFTES contents under the temperature from  $-20^\circ\text{C}$  and  $20^\circ\text{C}$ . Fig. 9 shows the trend graphs of CA and SA on the superhydrophobic surfaces in different temperatures. Significant changes of CA and SA on the surface are observed after lowering the temperature. For all of the samples, it can be seen from Table 4 that the CA on the hybrid colloid surface decreased, while SA increased obviously with decreasing temperatures. For the colloid coating sample of HFTES-6 wt%, the CA on the surface declined to about  $136^\circ$  and SA increased to  $41^\circ$  under  $-20^\circ\text{C}$ . This result indicates that the wettability of the coating surface distinctly increased under lower temperatures.

Surprisingly, as the surface temperature varied from  $20^\circ\text{C}$  to  $-20^\circ\text{C}$ , the change range of CA and SA on the colloid film with high fluorine contents is visibly less than that with low fluorine contents. For the sample of HFTES-30 wt%, the CA on the surface remain at about  $161^\circ$  and SA at  $9^\circ$  under  $-20^\circ\text{C}$ . This behavior indicates that the surface covered with more fluorinated groups exhibit superior hydrophobicity under lower temperature. The changes of CA and SA on the samples of HFTES-30 wt% and HFTES-40 wt% have the same tendency with the decreasing temperature. This is mainly attributed to almost the same surface composition for these two coating samples as demonstrated in XPS analysis.

Water condensation is believed to be the principal reason for increased wettability of superhydrophobic surfaces characterized by descending CA and ascending SA.<sup>49</sup> At room temperature, water droplets on the fluorinated films with a micro-nano

**Table 3** Contact angle (CA), advancing contact angle ( $\theta_A$ ), receding contact angle ( $\theta_R$ ), contact angle hysteresis (CAH) and sliding angle (SA) of water on the colloid surfaces containing different HFTES contents<sup>a</sup>

Sample	CA ( $^\circ$ )	$\theta_A$ ( $^\circ$ )	$\theta_R$ ( $^\circ$ )	CAH ( $^\circ$ )	SA ( $^\circ$ )
HFTES-0 wt%	98.67	N/A	N/A	N/A	N/A
HFTES-1 wt%	120.31	148.48	96.31	52.17	51
HFTES-3 wt%	140.48	139.73	98.52	41.21	36
HFTES-5 wt%	158.25	160.19	147.57	12.62	13
HFTES-6 wt%	166.93	168.88	163.56	5.32	4
HFTES-10 wt%	166.97	169.05	163.78	5.27	4
HFTES-30 wt%	167.04	169.27	162.94	6.33	5
HFTES-40 wt%	166.88	170.11	161.65	8.46	6

<sup>a</sup> N/A: no angles were recorded. The droplet did not roll off even at a  $90^\circ$  tilting angle.

**Table 4** CA and SA of water on different fluorinated superhydrophobic surfaces from  $-20^\circ\text{C}$  to  $20^\circ\text{C}$  with relative humidity of 40%

Temperature ( $^\circ\text{C}$ )	HFTES-6 wt%		HFTES-10 wt%		HFTES-30 wt%		HFTES-40 wt%	
	CA ( $^\circ$ )	SA ( $^\circ$ )	CA ( $^\circ$ )	SA ( $^\circ$ )	CA ( $^\circ$ )	SA ( $^\circ$ )	CA ( $^\circ$ )	SA ( $^\circ$ )
20	166.93	4	166.97	4	167.04	5	166.88	6
10	164.52	7	164.93	6	166.36	5	166.24	6
0	158.11	12	160.85	10	165.43	6	164.97	7
-10	149.05	23	154.48	15	163.82	7	162.96	8
-20	136.39	41	144.52	27	161.61	9	160.84	10

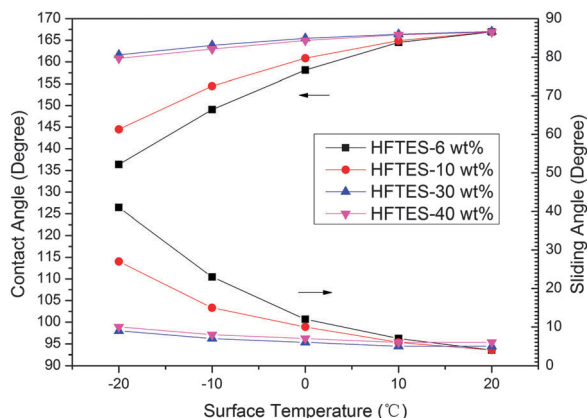


Fig. 9 Trend Graphs of CA and SA of the superhydrophobic colloid surfaces containing various amounts of HFTES at different temperatures with a relative humidity of 50%.

composite structure can be considered to appear as the Cassie–Baxter state. However, condensation of water under low temperature might convert a drop from the Cassie–Baxter state to the Wenzel state. Fig. 10 illustrates the water droplets on the colloid superhydrophobic surfaces containing different fluoride contents under an overcooled and humid condition. The temperature difference ( $\Delta T$ ) between the coating surface and the dew point is essential to decide whether water vapor in the atmosphere condenses into liquid on the surface.<sup>39</sup> When surface temperature decreased under high humidity, the  $\Delta T$  gradually decreased, indicating a promoted possibility of condensation on cold substrates. High fluorinated group covered surface is known as the most difficult to undergo wetting. The outstanding water repellence property improves the barrier for the transition of the surface wetting state from the Cassie–Baxter mode to the Wenzel mode. The condensation water on this superhydrophobic

surface will coalesce and combine into microdroplets, which can be suspended on the micro-nano composite surface with high fluorine contents even at lower temperature. Only the samples with HFTES contents above 30 wt% possess relatively stable water repellent property under the temperature range of  $-20$ – $20$  °C.

**3.4.3 Delay in the crystallization of condensed water.** Water droplet on the superhydrophobic surface has less intimate contact with the solid surface because of the vapor pockets existing at the solid–water interface in the Cassie–Baxter state, which makes the droplet easy to roll off. However, the condensation of water followed by crystallization will occur on superhydrophobic surfaces in practical application of anti-icing coatings under cold and humid environments. The delayed freezing time of supercooled water on the coating surface is another important indicator for the anti-icing property. As discussed above, superhydrophobic surfaces showed various wetting properties under different temperature conditions. The wettability at subzero temperature may really affect anti-icing properties of surfaces. Fig. 11 shows the photographs of individual water droplets on uncoated glasses and colloid superhydrophobic surfaces containing different HFTES contents in the whole freezing process at  $-20$  °C by a high speed CCD camera of CAM 200 optical contact-angle goniometer.

It can be observed in Fig. 11 that the transparent center of the condensed water vanished when the water began to freeze because of the difference in reflectivity. The recorded data demonstrate that superhydrophobic surfaces with different fluorine contents showed various freezing delay time. As the HFTES content increased, the freezing delay time for the superhydrophobic surface became longer compared with the uncoated hydrophilic glass. The freezing delay time reached 1776 s and 1760 s for the coating samples HFTES-30 wt% and HFTES-40 wt%. This result further indicates that more

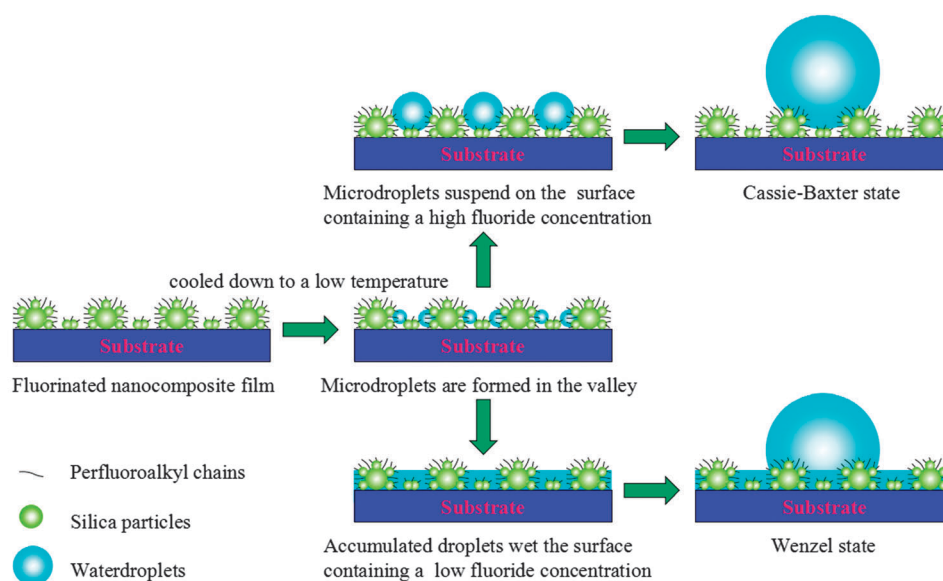


Fig. 10 Schematic illustration of water droplets on the colloid superhydrophobic surfaces containing fluoride content in high- and low-level under overcooled and humid conditions.



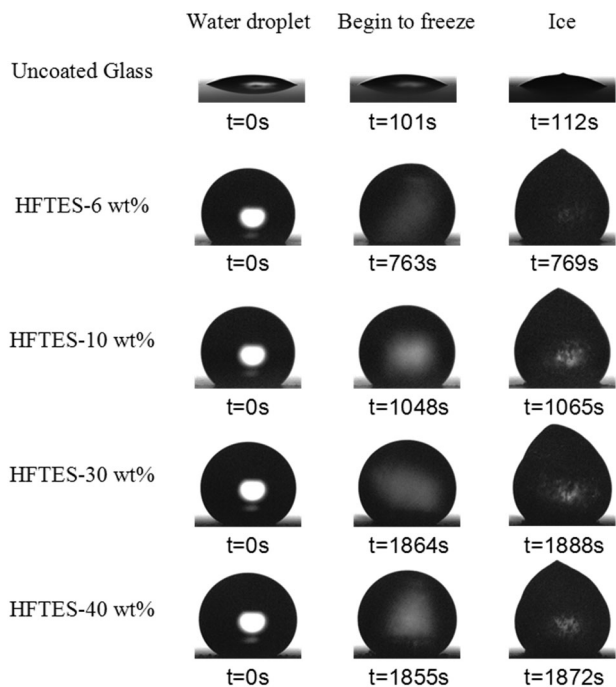


Fig. 11 Photographs of individual water droplets on glasses with different coatings during the whole freezing process captured by a high speed CCD camera of CAD 200 optical contact-angle goniometer. The silica contents is 30 wt% for all of the samples.

fluorinated group covered surfaces are more suitable for preventing ice formation. In general, ice formation of water droplets on the cooled superhydrophobic surface undergo water cooling and nucleation processes. The freezing rate of the condensation water is mainly influenced by the heat conduction rate from that to the substrate. The heat transfer through conduction between the interface of the water droplet and the coating surface can be described as the following equation:

$$dQ/dt = -HA(T_2 - T_1) \quad (1)$$

where  $dQ/dt$  = heat transfer rate ( $\text{J s}^{-1}$ ),  $H$  = heat transfer constant ( $\text{J m}^{-2} \text{s}^{-1} \text{K}^{-1}$ );  $A$  = interfacial area ( $\text{m}^2$ ); and  $T_1$  and  $T_2$  = the initial and final temperatures (K).

The heat transfer rate between the droplet-substrate interfaces is related to the contact area. A reduced contact area is inevitable in the case of the superhydrophobic surface with a high contact angle. Moreover, the superhydrophobic surfaces with micro-nano composite roughness possess an air fraction with inherent insulating properties. For the same volume of water droplets, the heat loss of water droplets is relatively slow on the superhydrophobic surface with the Cassie-Baxter state compared to one residing in the Wenzel state. Besides the heat transfer, the nucleation mechanism of ice in the water droplets also can affect the freezing delay time. Heterogeneous nucleation of condensation water often occurs on top of the superhydrophobic surface with uniform low surface energy. The energy barrier for heterogeneous nucleation on the superhydrophobic rough surfaces is much lower than that in the case of homogeneous nucleation on the smooth surface. Furthermore, a

Table 5 CA, SA and freezing delay time test of sample HFTES-30 wt%– $\text{SiO}_2$ -30 wt% at  $-20^\circ\text{C}$ , before and after multiple icing/de-icing cycles

Icing/de-icing cycles	CA ( $^\circ$ )	SA ( $^\circ$ )	Freezing delay time (s)
0	161.61	9	1776
5	159.36	13	1747
10	158.84	17	1651

water droplet must overcome the potential barrier to crystallize. According to the classic nucleation theory,<sup>49</sup> the free barrier for heterogeneous nucleation ( $\Delta G$ ), which is the Gibbs free energy of formation of spherical crystals with radius  $R$  from the supercooled water droplet, can be calculated by the following equations.

$$\Delta G = \left( \frac{2\pi R^3}{3} \Delta g + 2\pi R^2 \gamma_{sl} \right) f(\theta) \quad (2)$$

$$f(\theta) = \frac{(2 + \cos \theta)(1 - \cos \theta)^2}{4} \quad (3)$$

where  $R$  is the droplet radius;  $\gamma_{sl}$  is the solid-liquid interfacial tension;  $\Delta g$  is the Gibbs's energy density difference between ice and liquid. It is worth noting that  $\theta$  may be the apparent contact angle in the current surface temperature. According to this equation,  $\Delta G$  is positively proportional to  $f(\theta)$ , which means that the bigger  $\theta$  is, the higher  $\Delta G$  is. The functional relation of eqn (3) shows that  $f(\theta)$  is monotonously increasing with  $\theta$ , the growing contact angle will raise the nucleation free energy barrier and retard the crystallization of condensed water. For the prepared superhydrophobic coating samples of HFTES-30 wt% and HFTES-40 wt% in this study, CA of water remains above  $160^\circ$  in the temperature range of  $-20$ – $20^\circ\text{C}$  and the water drops roll on the surface with SA below  $10^\circ$ . Therefore, these two colloid coating samples with high fluorine contents were more effective in delaying the freezing time.

The stability of the sol-gel coating was examined by wettability and anti-icing tests during 10 icing/ice-melting cycles. The results of sample HFTES-30 wt%– $\text{SiO}_2$ -30 wt% are listed in Table 5. The sample keeps excellent superhydrophobic and anti-icing properties in 10 icing/de-icing cycles. It is showed that the prepared colloid surface lost part of its superhydrophobicity with CA decreased from  $161.61^\circ$  to  $158.28^\circ$ , and SA increased from  $9^\circ$  to  $17^\circ$ , respectively, after 10 icing/ice-melting cycles. The change of superhydrophobic property results in deterioration of anti-icing performance with freezing delay time decreased from 1776 s to 1651 s. This result indicates that the coating possess good durability for anti-icing application.

## 4. Conclusions

In this work, the micro-nano roughness structure for the prepared colloid films with superhydrophobic property was efficiently prepared by hydrolytic condensation of MTES, HFTES and nanosilica sol. The effect of surface multiscale roughness and fluorinated groups on the wettability of the prepared surfaces was investigated by a water contact angle and sliding angle test. The fabricated

colloid surface with low HFTES contents achieved superhydrophobic property at ambient temperature because of the significant surface enrichment of fluorinated groups. Surface morphology and XPS study indicate that both roughness and fluoride contents are key factors on the superhydrophobic performance. Only the coating films with HFTES contents above 30 wt% exhibit special superhydrophobic and anti-icing properties under freeze temperature. The droplets of overcooled water can easily roll off the surface before freezing. More fluorinated groups covered surface raise the barrier for the transition of the surface wetting state from the Cassie–Baxter mode to the Wenzel mode. Superhydrophobic colloid film containing above 30 wt% HFTES shows the best anti-icing property in our study by delaying freezing time to 1888 s at  $-20^{\circ}\text{C}$ . Compared with the influence of the surface roughness, the high fluoride enrichment on the surface plays the major role in anti-icing properties under overcooled conditions. What's more, the superhydrophobic and anti-icing film showed good adhesion strength to substrate and good performance of icing/ice-melting cycles. The findings of this study offer a facile strategy for fabricating a surface with superhydrophobic and anti-icing properties under extreme weather conditions.

## Acknowledgements

The authors would like to gratefully acknowledge the National Natural Science Foundation of China (NSFC) for Award No. 21276224, 21476195 and Zhejiang Provincial Natural Science Foundation of China for Award No. Y14B060038 for supporting this research.

## Notes and references

- 1 S. Jung, M. K. Tiwari, N. V. Doan and D. Poulikakos, *Nat. Commun.*, 2012, **3**, 615.
- 2 J. Chen, Z. Luo, Q. Fan, J. Lv and J. Wang, *Small*, 2014, **10**, 4693–4699.
- 3 O. Parent and A. Ilinca, *Cold Reg. Sci. Technol.*, 2011, **65**, 88–96.
- 4 S. A. Kulinich, M. Honda, A. L. Zhu, A. G. Rozhin and X. W. Du, *Soft Matter*, 2015, **11**, 856–861.
- 5 S. Chernyy, M. Järn, K. Shimizu, A. Swerin, S. U. Pedersen, K. Daasbjerg, L. Makkonen, P. Claesson and J. Iruthayaraj, *ACS Appl. Mater. Interfaces*, 2014, **6**, 6487–6496.
- 6 Y. Wang, M. Li, T. Lv, Q. Wang, Q. Chen and J. Ding, *J. Mater. Chem. A*, 2015, **3**, 4967–4975.
- 7 X. Zhan, Y. Yan, Q. Zhang and F. Chen, *J. Mater. Chem. A*, 2014, **2**, 9390–9399.
- 8 Y. Wang, J. Xue, Q. Wang, Q. Chen and J. Ding, *ACS Appl. Mater. Interfaces*, 2013, **5**, 3370–3381.
- 9 W. Barthlott and C. Neinhuis, *Planta*, 1997, **202**, 1–8.
- 10 W. Li and A. Amirfazli, *Adv. Mater.*, 2007, **19**, 3421–3422.
- 11 G. McHale, N. J. Shirtcliffe and M. I. Newton, *Langmuir*, 2004, **20**, 10146–10149.
- 12 T. Darmanin, E. T. de Givenchy, S. Amigoni and F. Guittard, *Adv. Mater.*, 2013, **25**, 1378–1394.
- 13 Y. Rahmawan, L. Xu and S. Yang, *J. Mater. Chem. A*, 2013, **1**, 2955–2969.
- 14 H. Bellanger, T. Darmanin, E. T. de Givenchy and F. Guittard, *Chem. Rev.*, 2014, **114**, 2694–2716.
- 15 Y. Liu, L. Moevius, X. Xu, T. Qian, J. M. Yeomans and Z. Wang, *Nat. Phys.*, 2014, **10**, 515–519.
- 16 P. Kim, M. J. Kreder, J. Alvarenga and J. Aizenberg, *Nano Lett.*, 2013, **13**, 1793–1799.
- 17 H. S. Salapare, F. Guittard, X. Noblin, E. Taffin De Givenchy, F. Celestini and H. J. Ramos, *J. Colloid Interface Sci.*, 2013, **396**, 287–292.
- 18 H. Li, Y. H. Zhao and X. Y. Yuan, *Soft Matter*, 2013, **9**, 1005–1009.
- 19 T. Darmanin and F. Guittard, *J. Mater. Chem.*, 2009, **19**, 7130–7136.
- 20 Q. F. Xu, J. N. Wang, I. H. Smith and K. D. Sanderson, *Appl. Phys. Lett.*, 2008, **93**, 233112.
- 21 M. Yoon, Y. Kim and J. Cho, *ACS Nano*, 2011, **5**, 5417–5426.
- 22 S. Sunny, N. Vogel, C. Howell, T. L. Vu and J. Aizenberg, *Adv. Funct. Mater.*, 2014, **24**, 6658–6667.
- 23 M. Ma, Y. Mao, M. Gupta, K. K. Gleason and G. C. Rutledge, *Macromolecules*, 2005, **38**, 9742–9748.
- 24 T. Ishizaki, J. Hieda, N. Saito, N. Saito and O. Takai, *Electrochim. Acta*, 2010, **55**, 7094–7101.
- 25 F. Palumbo, R. Di Mundo, D. Cappelluti and R. D'Agostino, *Plasma Processes Polym.*, 2011, **8**, 118–126.
- 26 A. K. Gnanappa, D. P. Papageorgiou, E. Gogolides, A. Tserepi, A. G. Papathanasiou and A. G. Boudouvis, *Plasma Processes Polym.*, 2012, **9**, 304–315.
- 27 T. Darmanin and F. Guittard, *Soft Matter*, 2013, **9**, 1500–1505.
- 28 J. Yang and W. Li, *J. Alloys Compd.*, 2013, **576**, 215–219.
- 29 R. V. Lakshmi, P. Bera, C. Anandan and B. J. Basu, *Appl. Surf. Sci.*, 2014, **320**, 780–786.
- 30 M. Hikita, K. Tanaka, T. Nakamura, T. Kajiyama and A. Takahara, *Langmuir*, 2005, **21**, 7299–7302.
- 31 H. Wang, J. Fang, T. Cheng, J. Ding, L. Qu, L. Dai, X. Wang and T. Lin, *Chem. Commun.*, 2008, 621–633.
- 32 J. Fang, H. Wang, Y. Xue, X. Wang and T. Lin, *ACS Appl. Mater. Interfaces*, 2010, **2**, 1449–1455.
- 33 Y. Zhao, J. Fang, H. Wang, X. Wang and T. Lin, *Adv. Mater.*, 2010, **22**, 707–710.
- 34 J. Liang, Y. Hu, Y. Wu and H. Chen, *Surf. Coat. Technol.*, 2014, **240**, 145–153.
- 35 B. J. Privett, J. Youn, S. A. Hong, J. Lee, J. Han, J. H. Shin and M. H. Schoenfish, *Langmuir*, 2011, **27**, 9597–9601.
- 36 C. Sanchez, B. Julián, P. Belleville and M. Popall, *J. Mater. Chem.*, 2005, **15**, 3559–3592.
- 37 S. Jung, M. Dorrestijn, D. Raps, A. Das, C. M. Megaridis and D. Poulikakos, *Langmuir*, 2011, **27**, 3059–3066.
- 38 S. A. Kulinich, M. Honda, A. L. Zhu, A. G. Rozhin and X. W. Du, *Soft Matter*, 2015, **11**, 856–861.
- 39 L. Yin, Y. Wang, J. Ding, Q. Wang and Q. Chen, *Appl. Surf. Sci.*, 2012, **258**, 4063–4068.

- 40 J. M. Campbell, F. C. Meldrum and H. K. Christenson, *J. Phys. Chem. C*, 2015, **119**, 1164–1169.
- 41 H. Lehmler, V. V. V. N. Rama Rao, D. Nauduri, J. D. Vargo and S. Parkin, *J. Fluorine Chem.*, 2007, **128**, 595–607.
- 42 T. H. Wu, A. Foyet, A. Kodentsov, L. G. J. van der Ven, R. A. T. M. van Benthem and G. de With, *Mater. Chem. Phys.*, 2014, **145**, 342–349.
- 43 K. Honda, M. Morita, H. Otsuka and A. Takahara, *Macromolecules*, 2005, **38**, 5699–5705.
- 44 T. Darmanin and F. Guittard, *Soft Matter*, 2013, **9**, 1500–1505.
- 45 N. L. Stock, V. I. Furdui, D. C. G. Muir and S. A. Mabury, *Environ. Sci. Technol.*, 2007, **41**, 3529–3536.
- 46 Q. Wang, Q. Zhang, X. Zhan and F. Chen, *J. Polym. Sci., Part A: Polym. Chem.*, 2010, **48**, 2584–2593.
- 47 Q. F. Xu, J. N. Wang and K. D. Sanderson, *ACS Nano*, 2010, **4**, 2201–2209.
- 48 A. V. Rao, A. B. Gurav, S. S. Latthe, R. S. Vhatkar, H. Imai, C. Kappenstein, P. B. Wagh and S. C. Gupta, *J. Colloid Interface Sci.*, 2010, **352**, 30–35.
- 49 K. K. Varanasi, M. Hsu, N. Bhate, W. Yang and T. Deng, *Appl. Phys. Lett.*, 2009, **95**, 94101.